

Iron incorporation in synthetic precipitated calcium silicate hydrates

Jirawan Siramanont^{a,b}, Brennan J. Walder^{c,1}, Lyndon Emsley^c, Paul Bowen^{a,*}

^a Laboratory of Construction Materials, Institut des Matériaux, Ecole Polytechnique Fédérale de Lausanne (EPFL), CH-1015 Lausanne, Switzerland

^b SCG CEMENT Co., Ltd., Saraburi 18260, Thailand

^c Laboratory of Magnetic Resonance, Ecole Polytechnique Fédérale de Lausanne (EPFL), CH-1015 Lausanne, Switzerland

ARTICLE INFO

Keywords:

Precipitation

Synthetic calcium silicate hydrates (C-S-H)

Ferrihydrite

Iron-containing siliceous hydrogarnet

ABSTRACT

Effect of Fe^{3+} on the precipitation of synthetic calcium silicate hydrates (C-S-H) under controlled conditions has been evaluated. Using extremely basic either initial calcium nitrate or sodium silicate solutions ($\text{pH} > 11$), incipient formation of ferrihydrite in both solutions was observed. In this case both C-S-H and iron-containing siliceous hydrogarnet are formed. For $\text{pH} < 11$, ferrihydrite was absent. Only C-S-H is formed. The presence of magnetically dilute Fe^{3+} in the C-S-H was shown by EPR and the atomic Fe/Si ratio of the C-S-H phase was shown to be between 0.01% and 0.1% by measuring and modelling the ^{29}Si spin-lattice relaxation in NMR experiments. A uniform distribution of Fe^{3+} when C-S-H precipitates in the absence of initial ferrihydrite is obtained. When initial ferrihydrite is present, a non-uniform distribution of Fe^{3+} is found and the concentration of Fe^{3+} in the C-S-H is merely 3% of the overall iron concentration, suggesting the initial formation of ferrihydrite restricts the incorporation of iron into C-S-H.

1. Introduction

Supplementary cementitious materials (SCMs) such as fly ash, calcined clays, ground granulated blast furnace slag and silica fume are commonly used for clinker substitution in blended cements. The percentage of clinker replacement (approximately 5–20%) reduces CO_2 emissions linked to the production of clinker [1–3]. Each of these SCMs have different chemical compositions which can result in different reactivities and the formation of different hydrated phases. Thus using SCMs makes concrete more sustainable; however, interaction of SCMs with Portland cement can affect reactivity and performance at early ages, which can reduce strength, an undesired behavior [2,4,5].

The major anhydrous phases in Portland cement, are alite (Ca_3SiO_5) and belite (Ca_2SiO_4). The minor phases are calcium aluminate ($\text{Ca}_3\text{Al}_2\text{O}_6$), ferrite ($\text{Ca}_2(\text{Al,Fe})_2\text{O}_5$), calcite (CaCO_3) and gypsum (CaSO_4) [1,2,6]. When cement reacts with water, various ions (e.g. Ca, Si, Al, Fe and hydroxide) release continuously into the pore solution forming various hydration products [7,8]. The main hydration products are calcium silicate hydrates (C-S-H), portlandite ($\text{Ca}(\text{OH})_2$), ettringite, calcium monosulphoaluminate or calcium monocarboaluminate. Typically, Portland cement contains approximately 2–5% of Fe_2O_3 . Iron-containing phases such as AFm phases are not very stable and can

transform to stable Al–Fe siliceous hydrogarnet phases during hydration [6,9,10]. Furthermore, metastable ferrihydrite (FeOOH) is often formed as an intermediate phase in the early stage of hydration, eventually transforming into siliceous hydrogarnet.

Calcined clay minerals, which when used in cement can lower the clinker factor, are often associated with relatively high Fe_2O_3 the content (0.3–15.4%) [11] which depends on the source of material. Chakchouk et al. [12] reported 5.87% of Fe_2O_3 in Tunisian clay and Danner et al. [13] found 10.6% of calcined marl in Norway. Ghorbel and Samet [14] investigated the pozzolanic activity of kaolin by varying iron contents in blended white cements. The pozzolanic activity was enhanced when adding iron up to 2.7% Fe_2O_3 , where compressive strength increased with a higher consumption of portlandite. Moreover, a dense structure of C-S-H and ettringite containing iron was observed by electron microscopy.

C-S-H is the major hydration product and the most important component in cement [15–17]. The volume of C-S-H is up to 50% of a fully hydrated cement paste [18]. It is a poorly crystalline non-stoichiometric material, which is difficult to characterize and describe at an atomistic level [15,17]. Solid-state ^{29}Si NMR has been among the most useful methods to study silicate arrangements in C-S-H [15,16,19,20]. For a given silicate unit this technique can be used to

* Corresponding author.

E-mail addresses: bwalder@sandia.gov (B.J. Walder), paul.bowen@epfl.ch (P. Bowen).

¹ Present address: Sandia National Laboratories, Department of Organic Materials Science, Albuquerque, NM 87185, USA.

describe the extent of bridging to other silicate units and the degree of silicate polymerization. The silica arrangement in C-S-H comprises parallel linear rows of silicate dimers, occasionally bridged together by another tetrahedron to create pentamers or longer oligomers. Such a “dreierketten” structure resembles the structure observed in some naturally occurring minerals such as tobermorite. 14 Å tobermorite is composed of calcium layers which are terminated on each side by silicate chains. Both Ca^{2+} and water can be found between these layers and it has been recently demonstrated from combined NMR and atomistic modelling that Ca^{2+} can in fact substitute the bridging silicate site in the silicate chain [15]. Furthermore, foreign ions such as Fe^{3+} , Al^{3+} and Zn^{2+} may be incorporated into C-S-H [21,22] but their exact position and nature are not fully understood. How such ions may affect the formation and growth of C-S-H has not been thoroughly investigated, often because of the complexity of cement hydration where more than eight solid phases can exist at any given time.

The aim of this work is to investigate the incorporation of Fe^{3+} ions into C-S-H prepared using the rapid precipitation method of Kumar et al. [15], who reported that uniform synthetic C-S-H with controlled Ca/Si ratios can be produced using a well-designed reactor with different precipitation modes. This reduces the chemical complexity of the products and allows us to identify the effect of individual parameters on nucleation and growth of synthetic C-S-H. The Ca/Si molar ratio of synthetic C-S-H can be controlled between 1.0 and 2.0 without the formation of any secondary phases. The addition of iron to the initial solutions will provide fundamental understanding on the role of Fe^{3+} on key factors like C-S-H formation which may influence early age properties while using SCMs containing iron. The resulting precipitates were fully characterized including magic-angle spinning (MAS) NMR, electron microscopy, electron paramagnetic resonance (EPR) spectroscopy and XRD, allowing us to determine the distribution and effects of iron in the products of the synthetic C-S-H precipitation system. Our results suggest the Fe^{3+} is incorporated into the C-S-H structure but is limited by the prior precipitation of a secondary phases such as ferrihydrite or hydrogarnet.

2. Materials and methods

2.1. Synthesis of pure phase C-S-H

The synthetic C-S-H was prepared via the dropwise method. A 0.1 M sodium silicate solution (Na_2SiO_3 , Sigma-Aldrich, CAS:6834-92-0) at pH 13.5 was present in the vessel and 0.2 M of calcium nitrate ($\text{Ca}(\text{NO}_3)_2 \cdot 4\text{H}_2\text{O}$, Fluka Chemicals, CAS:13477-34-4) at pH 6.5 was introduced into the vessel in a drop wise manner at a fixed rate of 2.17 mL/min. The pH of the solutions was adjusted by using sodium hydroxide (NaOH , Acros organic, CAS:1310-73-2) as indicated by Kumar et al. [15] to target a C-S-H with a Ca/Si ratio of 2.0. The total reaction time was 3 h. All solutions were prepared by using ultra-pure water previously boiled to remove dissolved CO_2 . After precipitation, the samples were washed with ultra-pure water mixed with ethanol (50:50 vol%) and followed by pure ethanol to remove unwanted ionic species in the precipitate. Then, samples were collected by vacuum filtration and stored as wet pastes in polystyrene containers.

2.2. Synthesis of C-S-H with Fe^{3+}

Iron (III) nitrate ($\text{Fe}(\text{NO}_3)_3 \cdot 9\text{H}_2\text{O}$, Acros Organics) solutions at pH 2.5 were used at 1.0 and 4.0 mM concentration (typical of calcined clay Fe contents) and added to either the initial sodium silicate solution or calcium nitrate solution. The synthetic conditions are summarized in Table 1. For samples Fe_A1, Fe_A2, Fe_B1, and Fe_B2, the precipitation of an Fe-containing phase was observed in the initial Fe containing solution with pH > 11. This is henceforth referred to as pre-precipitation as it occurred prior to precipitation of the C-S-H. The experimental conditions were modified by lowering the pH of the initial solution I to avoid

Table 1

Description of the solutions used in the precipitation of synthetic C-S-H in the presence of iron.

Sample	Initial solution I			Initial solution II		
	Ca (NO_3) ₂ ·4H ₂ O	Fe (NO_3) ₃ ·9H ₂ O	pH	Na ₂ SiO ₃	Fe(NO ₃) 3·9H ₂ O	pH
CSH	0.2 M	–	6.5	0.1 M	–	13.5
Fe_A1	0.2 M	1.0 mM	11.0	0.1 M	–	13.5
Fe_A2	0.2 M	4.0 mM	11.0	0.1 M	–	13.5
Fe_B1	0.2 M	–	6.5	0.1 M	1.0 mM	13.5
Fe_B2	0.2 M	–	6.5	0.1 M	4.0 mM	13.5
Fe_C1	0.2 M	1.0 mM	2.5	0.1 M	–	13.5
Fe_C2	0.2 M	4.0 mM	2.5	0.1 M	–	13.5

pre-precipitation for samples Fe_C1 and Fe_C2. The synthetic C-S-H with Fe^{3+} was synthesized via the dropwise method in the same manner as for the synthesis of the pure phase C-S-H, i.e. by adding dropwise initial calcium solution I to initial silicate solution II that was already in our reaction vessel.

2.3. Characterization methods

The morphology of samples was observed by transmission electron microscopy. A Thermo Scientific™ Talos F200X scanning transmission electron microscope was operated in high-resolution mode at 200 kV. TEM images were collected and then exported by using TEM Imaging and Analysis (TIA) software. The samples were prepared by dispersing the precipitated C-S-H in isopropanol and treated in an ultrasonic bath for 15 min. The dispersed samples were dropped onto the charged grid (carbon films on 300 mesh copper grids, Agar Scientific Ltd.) and allowed to dry for a few minutes. High angle annular dark field (HAADF) scanning transmission electron microscopy (STEM) combined with EDX was used to make an elemental mapping of the samples.

Synthetic C-S-H precipitates were dissolved in concentrated HNO_3 to determine the Ca/Si ratio and Fe content by inductively coupled plasma (ICP) on an ICPE-9000 series (Shimadzu) instrument. For characterization by XRD and TGA the C-S-H samples were freeze-dried for 24 h after washing. The freeze-drying was performed with Alpha 1–2 LD plus, Martin Christ Gefriertrocknungsanlagen GmbH. The filtered samples were kept in polystyrene containers at -80°C overnight. Then, the samples were put in glass containers and finally attached to the freeze dryer valve for 24 h. The diffractogram of the freeze-dried powder was measured using $\text{CuK}\alpha$ XRD (PANanalytical) with a fixed divergence slit. The size of the slit is $\frac{1}{2}$. The patterns were scanned for values of 2θ between 5° and 70° . Thermogravimetric analysis (TGA) was performed on a Mettler Toledo SDTA851 instrument using a temperature ramp from 30°C to 1000°C at $10^\circ\text{C}/\text{min}$ under a nitrogen atmosphere. The data presented is typical of two replicates.

Thermodynamic modelling has been carried out using the Gibbs free energy minimisation program GEMS [23,24]. This software package GEMS v.3 has been developed to compute the chemical speciation of the pore solution and hydrate phase assemblage during cement hydration. In our work, the *cem18* database was used for thermodynamic calculation. The activity model used was the extended Debye-Huckel with the associated values of the b_γ and a_0 values of 0.123 and 3.67 respectively. The C-S-H model used was the cshq model [23]. GEMS predicts possible equilibrium phases in our synthetic C-S-H system in the presence of Fe^{3+} .

X-band EPR experiments were carried out using the Bruker EMX Nano platform with a variable temperature (VT) accessory to lower the sample temperature to 100 K. The fixed operating frequency of the spectrometer was 9.60 GHz and the field was swept from 40 mT to 600 mT. For each analysis approximately 40 mg of sample was loaded into 3.2 mm outer diameter (OD) sapphire rotors capped with a PTFE insert and frozen directly in the VT accessory. A reference spectrum of the empty sample container at 100 K was used for background subtraction

and an additional third-order baseline correction was applied during processing.

Solid-state magic-angle spinning (MAS) NMR experiments were carried out at 21.14 T on a Bruker Avance Neo spectrometer. The samples were packed in 3.2 mm OD sapphire rotors capped with a PTFE insert and zirconia drive cap and spun at 12.5 kHz in a dynamic nuclear polarization MAS probe capable of lowering the sample temperature to 100 K. The ^{29}Si and ^1H rf field amplitudes were 66 kHz and 93 kHz, respectively, with the ^1H amplitude ramped from 90% to 100% during the 4 ms contact pulse used for cross-polarization (CP) enhancement of ^{29}Si signals prior to longitudinal storage using a z-filter. Multiple echo acquisition using the Carr-Purcell-Meiboom-Gill (CPMG) scheme was implemented during detection for further signal enhancement [25]. Integration of the CPMG signal across the ^{29}Si chemical shift region of C-S-H to obtain the normalized intensities used in the NMR determination of iron concentration in the C-S-H foils was done using the macOS application *RMN* [26]. Fitting the intensity data for the iron concentration was done with a script written for *gnuplot*.

3. Results

3.1. Morphology

TEM micrographs of the synthetic C-S-H samples are shown in Fig. 1 (low Fe content) and Fig. 2 (High Fe content). All samples exhibit C-S-H in the foil morphology, as expected for Ca/Si ratios around 2.0 [15]. Spherical nanoparticles roughly 100 nm in diameter are also observed for Fe_A2 (Fig. 2(a)) and Fe_B2 (Fig. 2(b)), when the samples prepared with high initial concentrations of Fe^{3+} . HAADF-STEM measurements combined with EDX were used to analyze the elemental distributions of samples Fe_C2 and Fe_B2, shown in Figs. 3 and 4, respectively. The HAADF image of Fe_C2, where the reaction conditions were such that pre-precipitation was avoided, shows C-S-H with a relatively homogeneous foil morphology. The distribution of Ca, Si and O are relatively uniform. The elemental map for Fe shows the iron is distributed over the whole sample, but some nonuniformity is suggested by bright regions observed in the mapping. These regions generally span 10 nm (occasionally up to 30 nm), suggesting some ultrafine Fe containing particles are embedded in the C-S-H foils. The HAADF-STEM-EDX measurements on sample Fe_B2 (Fig. 4) show the mixture of C-S-H foils and the large spherical nanoparticles that are well-evident in the TEM imagery. Uniform distributions of Ca, Si, and O are detected in both foils and

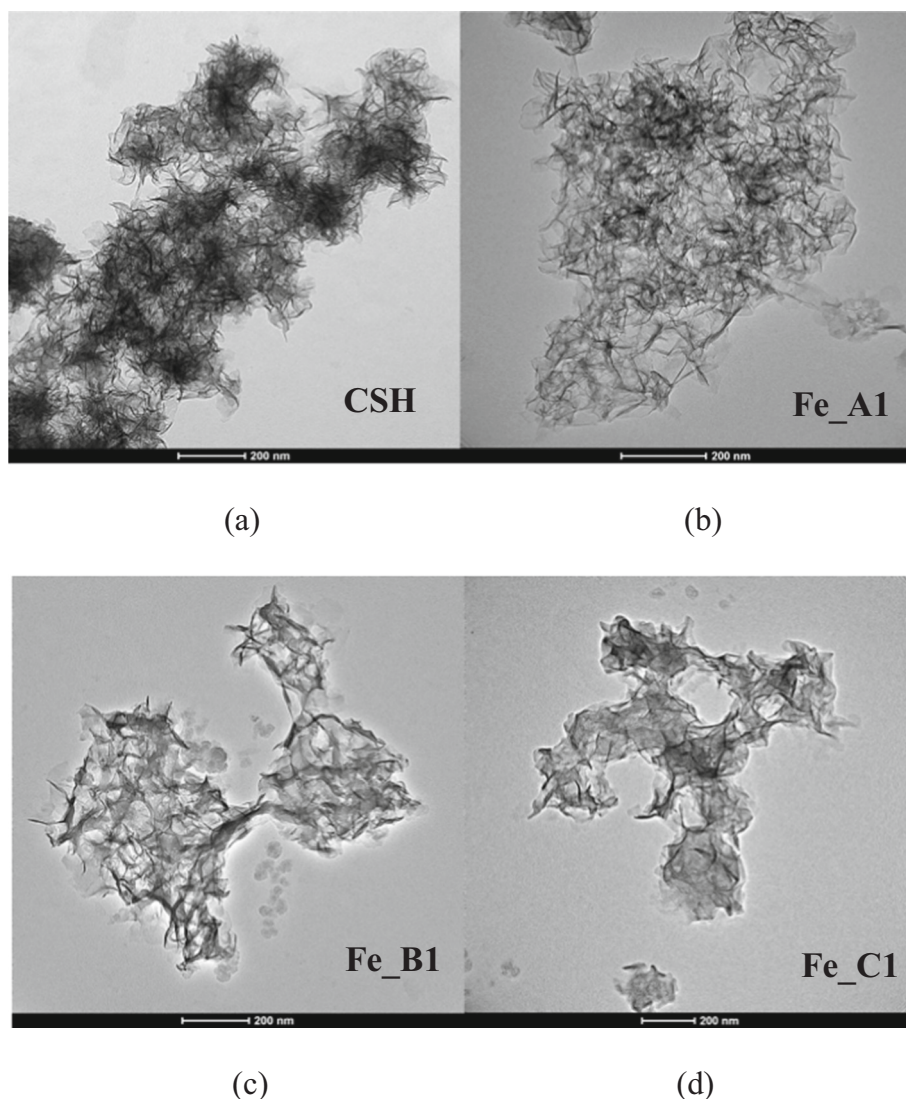


Fig. 1. Morphology of synthetic C-S-H (a) CSH, synthetic C-S-H with low concentration of Fe^{3+} (b) Fe_A1, (c) Fe_B1, (d) Fe_C1.

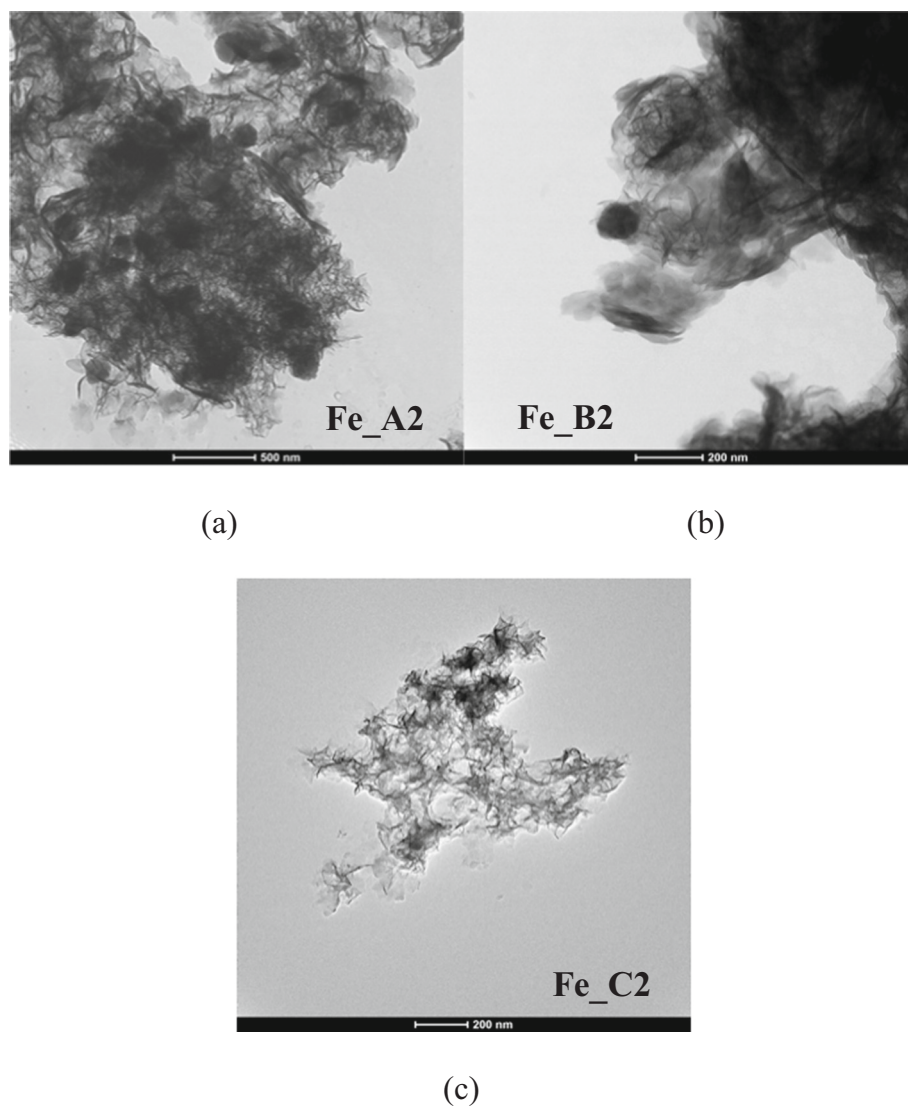


Fig. 2. Morphology of synthetic C-S-H with high concentration of Fe^{3+} (a) Fe_A2, (b) Fe_B2, (c) Fe_C2.

spherical nanoparticles. In contrast to the Fe_C2 sample, however, Fe is concentrated almost exclusively in the spherical nanoparticles. The C-S-H foils are of questionable visibility in the Fe mapping, and as such STEM-EDX analysis alone does not allow us to confidently establish the presence of iron in the C-S-H phase.

3.2. Chemical compositions

The Ca/Si ratio and Fe content for the precipitated synthetic C-S-H samples are shown in Table 2. The quantity of iron in the samples mainly depends on the Fe^{3+} concentration of the reactants. At low concentration of Fe^{3+} the C-S-H shows 0.010–0.014 mmol/g of Fe, whereas at high concentrations of Fe^{3+} there are 0.039–0.048 mmol/g of Fe, consisting of about 3% of the iron initially added to the reaction vessel. The presence of Fe^{3+} in the precipitation of the synthetic C-S-H leads to overall Ca/Si ratios in general lower than the pure C-S-H system. The Fe_B2 sample, where high initial Fe^{3+} concentration and pH led to significant pre-precipitation in the initial sodium silicate solution, is the most remarkable of these, exhibiting the lowest overall Ca/Si of around 1.2. This does not necessarily reflect the Ca:Si ratio of the C-S-H phase itself, owing to the significant amount of Ca and Si contained in the spherical nanoparticles.

3.3. XRD data

When preparing the initial Fe containing solutions for samples Fe_A1, Fe_A2, Fe_B1, and Fe_B2, pre-precipitation of an iron-containing phase occurred when the pH of the solution reached the designated pH shown in Table 1. The colour of the pre-precipitate in both initial solutions I and II was dark brown. The XRD pattern of the Fe-containing solution in the initial solution I and II after pre-precipitation is shown in Fig. 5. The lack of any well-defined peaks indicates that the dark brown solid is a poorly crystalline material. Given its characteristic colour, the precipitate is an iron-containing material such as ferrihydrite [27,28].

XRD analysis results for the seven synthetic C-S-H products show characteristic peaks for 2θ values of $16\text{--}18^\circ$, 29.2° , 33° , 50° , 55° and 67° , which corresponds well to dried synthetic C-S-H [16]. When comparing C-S-H in the presence of Fe^{3+} at low concentration (Fig. 6), all samples shows similar pattern to C-S-H except for a small broad peak around $2\theta = 17^\circ$, which, according to recent results from Grangeon et al. [16], corresponds to the occupancy of Si atoms in bridging sites of the silicate chains in C-S-H. At the higher Fe^{3+} concentration, (Fig. 7), the Fe_C2 sample also shows a similar pattern to pure C-S-H again with the small broad peak around $2\theta = 17^\circ$. On the other hand, Fe_A2 and Fe_B2 show additional crystalline peaks at 2θ values of 17.4° , 20.0° , 26.8° ,

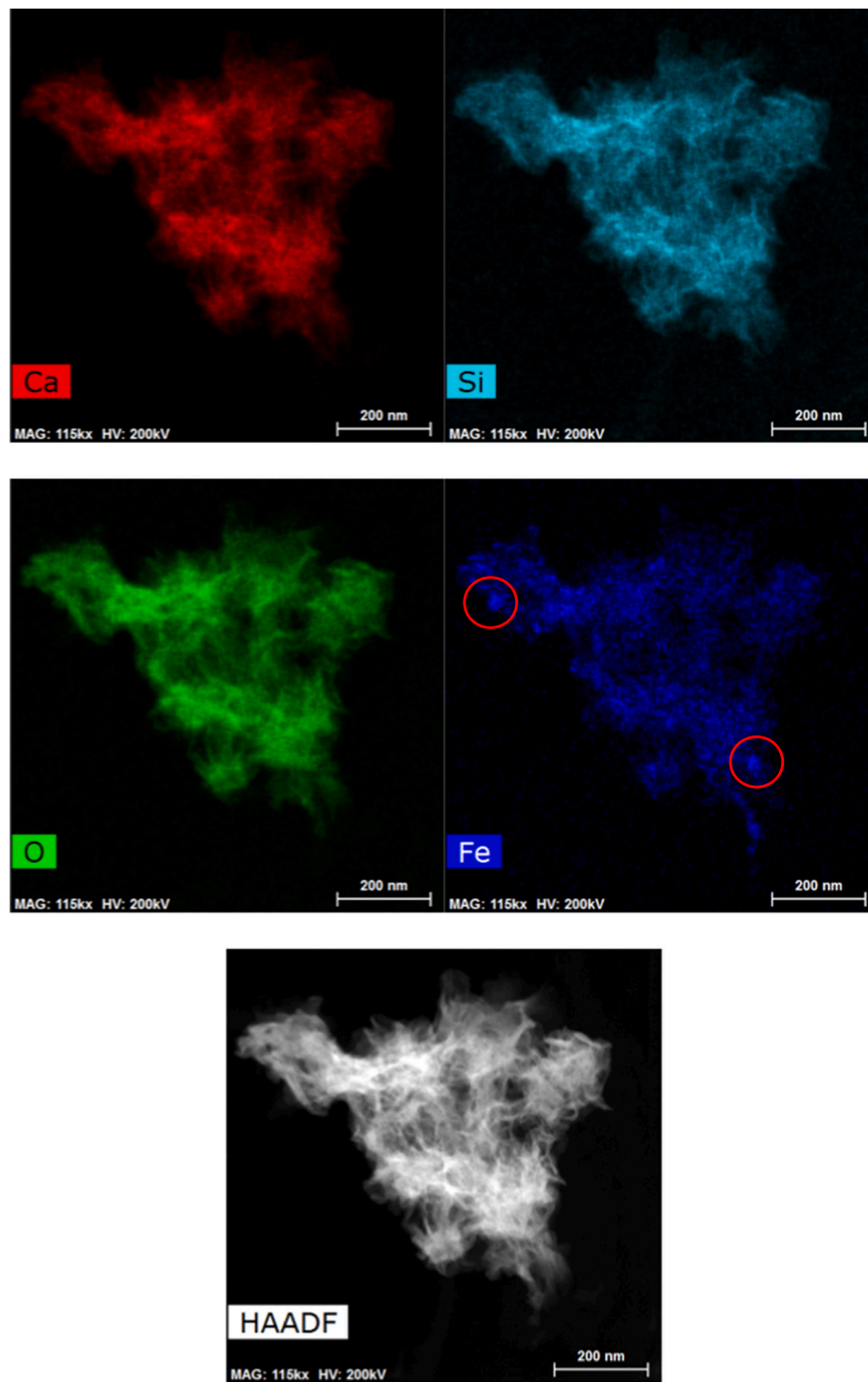


Fig. 3. STEM-EDX of synthetic C-S-H with high concentration of Fe^{3+} (Fe_C2). Bright regions spanning up to 30 nm in length suggest slight nonuniformity in the Fe distribution and are indicated by red circles in the Fe map. (For interpretation of the references to colour in this figure legend, the reader is referred to the web version of this article.)

28.7°, 33.0°, 35.2°, 39.6°, 44.7° and 52.9°, which correspond to siliceous hydrogarnet containing iron [29]. There are some small crystalline peaks of NaNO_3 at 23.2° and 48.4° and Ca(OH)_2 at 18.1°, 34.1° and 47.3° (20).

3.4. TGA data

TGA analysis of the samples are shown in Figs. 8 and 9. In cementitious materials, mass loss of samples up to 600 °C relate to the loss of

water and above 600 °C corresponding to the loss of CO_2 [30]. All freeze-dried samples show the main weight loss in TGA curve between 80 °C and 150 °C, typical of interlayer water in C-S-H. The broad weight loss between 650 °C and 700 °C could be due to poorly crystalline CaCO_3 . At high concentrations of Fe^{3+} (Fig. 9), there are weight losses at 320 °C approximately 2 wt.-%, and 450 °C approximately 5 wt.-%. These can be attributed to siliceous hydrogarnet containing iron [11] and Ca(OH)_2 , respectively. When analyzing wet samples (without freeze drying) we do not see any Ca(OH)_2 or CaCO_3 suggesting some minor degradation and

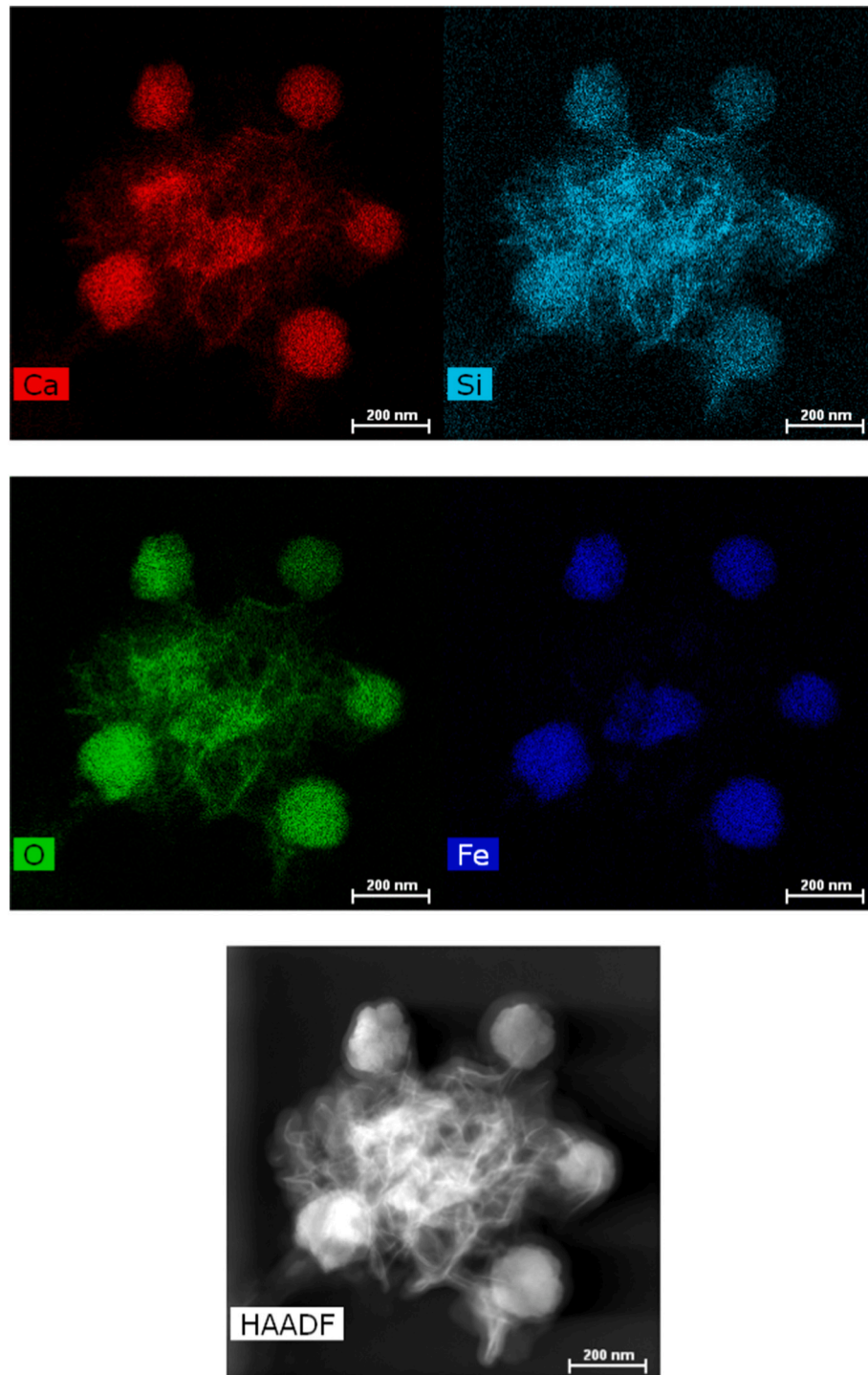


Fig. 4. STEM-EDX of synthetic C-S-H with high concentration of Fe^{3+} (Fe_B2).

Table 2

Ca/Si ratios and quantity of Fe per gram of sample from ICP measurements. The '±' represents the standard deviation of three individual measurements.

Sample	Ca/Si	Fe/Si	Fe/mmol/g
CSH	2.2 ± 0.6	—	—
Fe_A1	1.7 ± 0.3	0.0006	0.014
Fe_A2	1.7 ± 0.1	0.0027	0.048
Fe_B1	1.7 ± 0.3	0.0006	0.010
Fe_B2	1.2 ± 0.1	0.0025	0.039
Fe_C1	1.8 ± 0.1	0.0006	0.011
Fe_C2	2.2 ± 0.6	0.0027	0.039

formation of CaCO_3 and $\text{Ca}(\text{OH})_2$ can sometimes take place during the freeze-drying stage.

3.5. Thermodynamic modelling, GEMS

With an initial solution $\text{pH} \geq 11$, pre-precipitation of an iron-containing phase was observed, regardless of whether the ferric nitrate was added to the calcium nitrate or sodium silicate solution. The thermodynamic modelling (GEMS) predicts iron species and possible solid phases of the initial Fe containing solution, as shown in Fig. 10. We see that the solid phase of the initial solution (Fe_A1, Fe_A2, Fe_B1 and

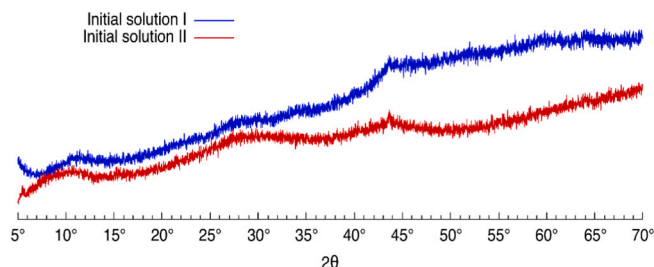


Fig. 5. XRD patterns of pre-precipitation of initial Fe containing solution in the initial solutions I and II.

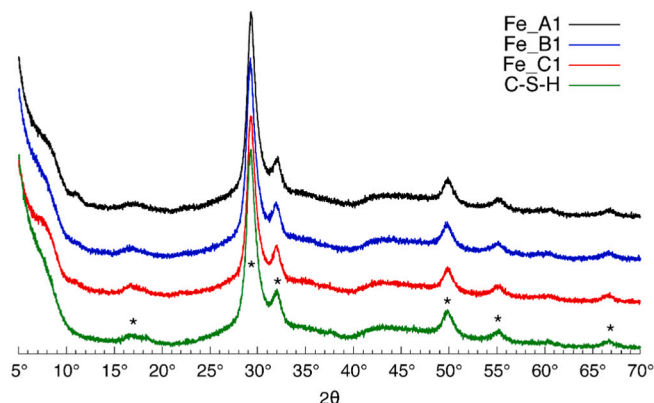


Fig. 6. XRD patterns of synthetic C-S-H and C-S-H synthesized in the presence of a low concentration of Fe^{3+} . (* - C-S-H).

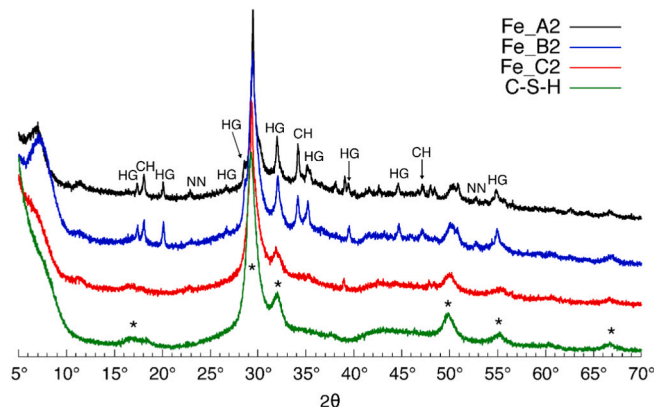


Fig. 7. XRD patterns of synthetic C-S-H and C-S-H synthesized in the presence of a high concentration of Fe^{3+} (HG-siliceous hydrogarnet, CH-calcium hydroxide and NN-sodium nitrate).

Fe B2) is expected to be ferrihydrite (FeOOH). The quantity of this phase depends on the concentration of Fe^{3+} and pH of the solution. Generally, Fe^{3+} is commonly used to prepare ferrihydrite precipitation in homogeneous solution which acts as a precursor of goethite synthesis [31–34]. Ferrihydrite is metastable and poorly crystalline, generally forming at $\text{pH} > 2.5$, preceding transformation to more crystalline and stable phases. At a pH of 2.5 for the initial solutions (Fe_C1, Fe_C2), there is no pre-precipitation of a solid phase. In this case, we see from Fig. 10 that the major Fe species in the initial solution are predicted to be Fe^{3+} , FeOH^{2+} , and $\text{Fe}_2(\text{OH})_4^{4+}$. From the thermodynamic modelling ferrihydrite (FeOOH) is not expected in the initial Fe containing solutions of Fe_C1 and Fe_C2, in agreement with our experimental findings.

The formation of C-S-H in the presence of Fe^{3+} was modelled using

GEMS. The possible solid phases and their quantities at equilibrium are shown in Table 3. GEMS only considers the final equilibrium point, and the matter whether the Fe^{3+} is considered to be added to the calcium nitrate or the sodium silicate is irrelevant here. In each case, C-S-H is the dominant solid phase in the system. In the presence of Fe^{3+} , GEMS predicts a second phase, an iron-containing siliceous hydrogarnet phase, $\text{Ca}_3\text{Fe}(\text{SiO}_4)_{0.84}(\text{OH})_{4.32}$. The calculations from GEMS shows good agreement with our experiments with high Fe^{3+} concentration of Fe_A2 and Fe_B2.

3.6. Electron paramagnetic resonance (EPR)

Further investigation into the speciation and distribution of iron in these samples was done using magnetic resonance. Fig. 11 shows low temperature X-band EPR spectra of two iron containing C-S-H samples prepared with and without pre-precipitation of ferrihydrite phases. The EPR spectrum of the sample Fe_C1 is dominated by a tall feature centered around an apparent g value of $g_{\text{eff}} = 4.3$. From this feature, a prominent wing extends toward lower field values, terminating at $g_{\text{eff}} = 9.7$. This broad pattern can be assigned to isolated Fe^{3+} ions ($S = 5/2$) in slightly distorted environments which lead to zero field splitting (ZFS)-induced displacements away from $g_{\text{eff}} = 2.0$ and into the low-field region. Such signals have a long history in the literature of silicates [35] and in the pioneering work of Castner et al. [36] it is proposed that they originate when Fe^{3+} substitutes for Si^{4+} in tetrahedral coordination as a network former. This remains circumstantial, however, since other configurations such as surface bound or solvated Fe^{3+} ions in the pore solution could conceivably lead to signals in this region and which would be nearly indistinguishable from those generated by bulk tetrahedral Fe^{3+} [37].

Toward higher field, a less distinct roll is visible as a minor feature, centered around $g_{\text{eff}} = 2$, which covers nearly the entire baseline to the upper end of the field sweep range (0.6 T, $g_{\text{eff}} = 1.1$). This is the result of iron centers in such proximity that the magnetic interaction between them becomes significant. This is expected in regions of higher iron density, an interpretation which is supported by the EPR spectrum of sample Fe_B2, which contain iron-rich nanoparticles. The broad feature at $g_{\text{eff}} = 2$ now dominates the spectrum, appearing as a rolling Gaussian line shape. The tall feature around $g_{\text{eff}} = 4.3$ due to isolated Fe^{3+} is a minor feature in comparison to the roll but remains visible nonetheless, suggesting that the sample does contain Fe^{3+} but at such a low concentration that the region is rendered dark in the Fe mapping by STEM-EDX.

3.7. Nuclear magnetic resonance (NMR)

Solid-state NMR is typically a method of choice for structural characterization, but can be challenging in samples containing iron due to signal quenching effects arising from strong magnetic couplings. We were able to observe the ^{29}Si nuclei in the C-S-H foil phase. High-resolution ^{29}Si spectra of Fe_B2, Fe_C1, and a C-S-H reference sample at a Ca:Si ratio of 2 are shown in Fig. 12. The ^{29}Si signals in each case correspond to the expected $Q^{(1)}$ (−79 ppm), $Q^{(2b)}$ (−82 ppm), and $Q^{(2p)}$ (−86 ppm) signals found in C-S-H, which partially overlap in yielding the NMR line shape characteristic to C-S-H. Because CP was used to measure these signals, the spectra in Fig. 12 are not quantitative, i.e. the ratio of the NMR signal intensities assigned to each Q species does not equal the corresponding atomic ratio of Q species in the C-S-H. Nonetheless, assuming the reference spectrum corresponds to a Ca:Si ratio of 2, the relatively small intensity of the $Q^{(2)}$ signals for Fe_B2 and the relatively large $Q^{(2)}$ signals for Fe_C1 would indicate Ca:Si ratios slightly larger and smaller than 2, respectively.

To selectively determine the concentration of Fe^{3+} in the C-S-H phase we measured the paramagnetic relaxation enhancement (PRE) of the ^{29}Si nuclei [38]. We accomplished this by measuring the decay of longitudinal ^{29}Si magnetization in z -filtered CP-MAS experiments as a

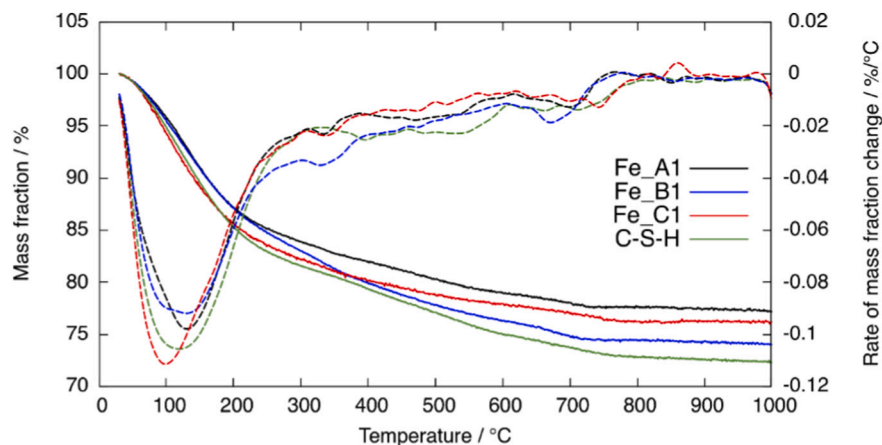


Fig. 8. TGA of synthetic C-S-H and C-S-H synthesized in the presence of a low concentration of Fe^{3+} . Solid curves correspond to mass fraction and dashed curves to the smoothed first derivative.

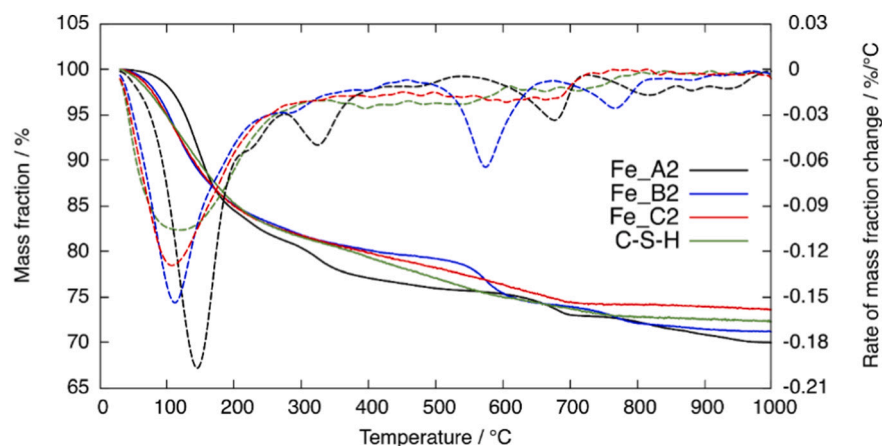


Fig. 9. TGA of synthetic C-S-H and C-S-H synthesized in the presence of a high concentration of Fe^{3+} . Solid curves correspond to mass fraction and dashed curves to the smoothed first derivative.

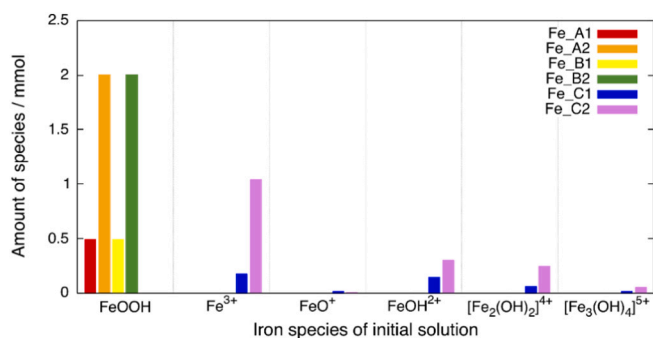


Fig. 10. Iron species of the initial Fe containing solution predicted from GEMS at equilibrium. The amount of Fe^{2+} , FeOH^+ , FeO_2^- , $\text{FeO}_2\text{H}\cdot\text{H}_2\text{O}$, $[\text{FeHSiO}_3]^{2+}$, and $\text{Ca}_3\text{Fe}(\text{SiO}_4)_{0.84}(\text{OH})_{4.32}$ species are predicted to be several orders of magnitude lower than those shown in the chart for each solution we consider.

function of longitudinal storage interval, τ_z . The intensities we measure are plotted in Fig. 13. We observe decays governed by multiexponential T_1 relaxation, mostly due to the wide distribution of ^{29}Si relaxation rates arising from the varied ^{29}Si - Fe^{3+} distances in our samples. Single exponential relaxation is a poor model of the decays we observe and hence we avoid providing explicit values of T_1 parameters in our discussion. We see that the ^{29}Si magnetization of C-S-H in the absence of

Table 3

Possible phases in synthetic C-S-H experiments with the presence of Fe^{3+} calculated by GEMS.

Sample	C-S-H (mM)	$\text{C}_3\text{FS}_{0.84}\text{H}_{4.32}$ (mM)
CSH	15.0	–
Fe_A1	14.8	0.2
Fe_A2	13.6	1.0
Fe_B1	14.8	0.2
Fe_B2	13.6	1.0

any added iron decays on the time scale of many hours, which may itself be due to residual paramagnetic impurities. The decay of ^{29}Si magnetization is an order of magnitude faster for the sample Fe_B2, which was prepared with high initial Fe^{3+} concentration and ferrihydrite pre-precipitation. Likewise, the ^{29}Si signal from the foils of Fe_C1, which was prepared at a lower Fe^{3+} concentration and without ferrihydrite pre-precipitation, decays yet another order of magnitude faster than Fe_B2, approaching zero after $\tau_z = 300$ s. This indicates that PRE is the dominant relaxation mechanism for the samples Fe_B2 and Fe_C1.

Our relaxation data can be quantitatively analyzed for the iron concentration of the C-S-H phase using a model which connects the density of iron centers to the signal decay by the PRE. Our NMR experiments were carried out at 100 K, 12.5 kHz MAS, and at the ^{29}Si natural abundance of 4.7%; therefore, we expect that molecular motion is effectively frozen and that ^{29}Si nuclear spin diffusion is exceedingly

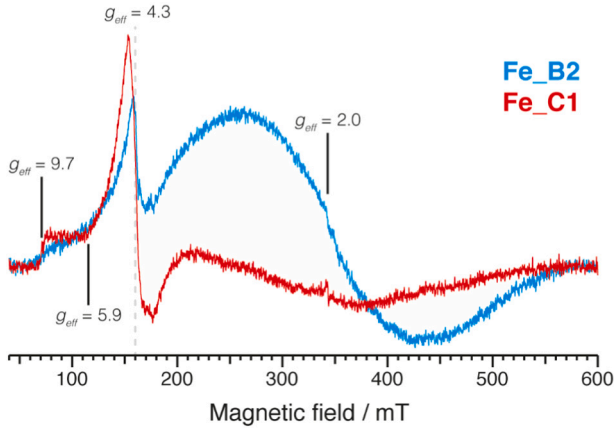


Fig. 11. X-band EPR spectra at 100 K of C-S-H samples synthesized with a high concentration of Fe^{3+} with pre-precipitation of ferrihydrite at a high Fe^{3+} concentration, Fe_B2; and without pre-precipitation at a low Fe^{3+} (1.0 mM in starting solution), Fe_C1.

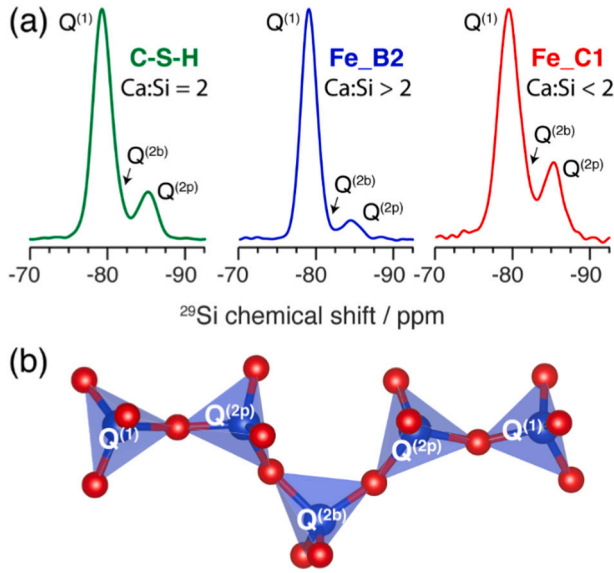


Fig. 12. (a) High-resolution ^{29}Si CP MAS NMR spectra of the C-S-H reference (green), Fe_B2 (blue), and Fe_C1 (red) at 21.14 T and a temperature of 100 K. The spectra are normalized with respect to the maximum height of the signal, which corresponds roughly to the height of the $\text{Q}^{(1)}$ signal at -79 ppm. (b) Structural schematic of a basic pentamer silicate chain in C-S-H with the Q speciation of each silicate identified. (For interpretation of the references to colour in this figure legend, the reader is referred to the web version of this article.)

slow. Neglecting these influences, the magnetization $M(r, \tau_z)$ at a distance r away from the nearest paramagnetic center is to a good approximation given by [39].

$$M(r, \tau_z) = (M(r, 0) - M_{\text{eq}}) \exp(-C\tau_z r^{-6}) + M_{\text{eq}}, \quad (1)$$

where M_{eq} is the equilibrium level of magnetization and C is a rate-related parameter [40,41]. In principle, Eq. (1) fails to describe the behavior of magnetization at sufficiently long τ_z , when more distant paramagnetic centers begin to affect the relaxation at a given point and the effects of nuclear spin diffusion can become significant [39,42]. Nevertheless, Labouriau, Kim and Earl showed in their ^{29}Si NMR study of Fe^{3+} in clays that in many practical cases a robust analysis can still be achieved assuming that the PRE by Fe^{3+} is governed by Eq. (1) at all

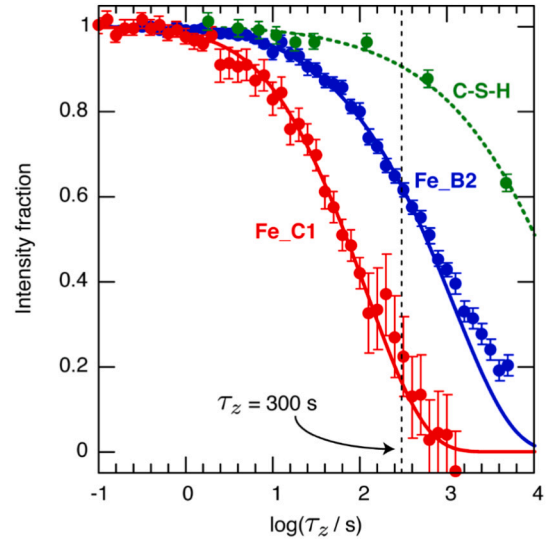


Fig. 13. Semi-log plot of the intensity of ^{29}Si signals as a function of the longitudinal storage interval τ_z at 21.14 T and 100 K for a reference sample of C-S-H synthesized in the absence of iron (green), Fe_B2 (blue) and Fe_C1 (red) at 100 K in the z-filtered CP experiment. The solid curves are the best fit of Eq. (2) to the data points where $\tau_z < 300$ s. The dashed green curve is fit to the entire dataset and is intended as a guide to the eye. Error bars correspond to 95% confidence intervals. (For interpretation of the references to colour in this figure legend, the reader is referred to the web version of this article.)

times [43]. Their model is equivalent to one in which the magnetization is contained within a single sphere, of radius R , whose volume is equal to the mean volume of C-S-H per Fe^{3+} center. This makes R the Wigner-Seitz radius of the Fe^{3+} dopants; by determining R , the concentration of iron follows. We also exclude magnetization within the quenching barrier radius b , for where $r < b$ there is no significant contribution to the NMR signal due to paramagnetic broadening effects. In adopting this single relaxation center model Eq. (1) can be integrated in the shell where $b < r < R$ and normalized under the approximation that the initial magnetization profile is uniform to obtain the analytic response function for our data,

$$S(\tau_z) = \frac{1}{R^3 - b^3} \left[R^3 \exp(-C\tau_z R^{-6}) - b^3 \exp(-C\tau_z b^{-6}) + \sqrt{\pi C\tau_z} \left(\text{erf}\left(\frac{\sqrt{C\tau_z}}{R^3}\right) - \text{erf}\left(\frac{\sqrt{C\tau_z}}{b^3}\right) \right) \right] \quad (2)$$

Labouriau, Kim, and Earl calibrated b by collating their MAS NMR results with independent analyses of Fe^{3+} concentration and found that $b = 1.0$ nm at 9.4 T and temperatures near 300 K. Adjusting this value to our magnetic field $B_0 = 21.14$ T and sample temperature $T = 100$ K according to the $B_0^{1/3}$ and $T^{1/3}$ dependencies of the barrier radius [39], we take $b = 1.89$ nm in Eq. (2) and jointly fit the relaxation data on Fe_B2 and Fe_C1 for the Fe^{3+} concentration (via $c[\text{Fe}^{3+}] = 3/(4\pi N_A R^3)$, where N_A is the Avogadro constant) and C . Our fit excludes the region where $\tau_z > 300$ s, when roughly 10% of the ^{29}Si magnetization in the iron-free C-S-H reference sample decays and relaxation by mechanisms other than PRE by Fe^{3+} may begin to contribute significantly. This also reduces the influence of any ^{29}Si nuclear spin diffusion. The result of this analysis is shown as the solid curves in Fig. 13. The best fit concentrations are, to 95% model confidence, $c[\text{Fe}^{3+}] = (2.4 \pm 0.6)$ mM for Fe_B2 and $c[\text{Fe}^{3+}] = (7.5 \pm 2.0)$ mM for Fe_C1, along with the joint fit parameter $C = (6.6 \pm 2.8)$ nm⁶/s. Assuming the chemical formula of the C-S-H phase is $(\text{CaO})_2(\text{SiO}_2) \cdot 1.9 \text{ H}_2\text{O}$ (neglecting the expected tiny Fe contribution) and the density of the C-S-H phase is 2.0 g/mL (not dried, [15]), these concentrations correspond to the atomic ratios $\text{Fe}/\text{Si} = (250 \pm 60)$ ppm and $\text{Fe}/\text{Si} = (770 \pm 210)$ ppm for Fe_B2 and Fe_C1, respectively.

For both samples, the fit to Eq. (2) is excellent in the region where $\tau_z < 300$ s. For $\tau_z > 300$ s, Eq. (2) is an extrapolation. We see that the extrapolation is good for Fe_C1, correctly predicting where the decay nears completion. Interestingly, this is not so for Fe_B2, where an increasingly positive deviation of $S(\tau_z)$ from the prediction emerges as τ_z increases. Indeed, at a τ_z of 5000 s, $S(\tau_z) \approx 0.20$, over twice the value predicted by our model of PRE relaxation. This suggests that for a significant portion of the C-S-H foils in Fe_B2, but not Fe_C1, the influence of PRE due to Fe^{3+} is not the same throughout the sample.

4. Discussion

In real Portland cement, ferrite is the major Fe phase which reacts with water forming ettringite, ferrihydrite and siliceous hydrogarnet containing iron. The ferrihydrite converts to more stable siliceous hydrogarnet in a few hours with increasing pH in the pore solution because of its metastable nature [6,10]. Fe enriched-kaolinite in blended white cement improves pozzolanic activity, for which an optimum level is 2.7% Fe_2O_3 [14]. A dense structure of C-S-H containing iron was found. At higher Fe_2O_3 contents, pozzolanic activity decreases and a new phase of $\text{AlCaFeS}(\text{OH})_5$ was observed.

Our results demonstrate the effect of Fe^{3+} , investigated at 1.0 and 4.0 mM, on the synthetic C-S-H via a dropwise precipitation method. This reflects a reduction in the chemical complexity relative to Portland cement blends. Nonetheless, multiple solid phases are sometimes observed. The precipitated C-S-H is the major phase and, occasionally, a prominent secondary phase of iron-containing siliceous hydrogarnet (Table 3). For Fe_A1 and Fe_A2, adding NaOH at pH 11.0 in the Ca and Fe solution leads to the pre-precipitation of ferrihydrite, which was predicted by thermodynamic calculations (Fig. 10) and observed as a poorly crystalline phase by XRD (Fig. 5). When the suspension of ferrihydrite in calcium drops into the silicate solution, the metastable ferrihydrite is expected, from thermodynamic modelling with GEMS, to transform to the more stable phase of siliceous hydrogarnet, $\text{Ca}_3\text{Fe}(\text{SiO}_4)_{0.84}(\text{OH})_{4.32}$. When adding NaOH to the Si and Fe solution (Table 1, Fe_B1 and Fe_B2), the iron again could be in the form of a pre-precipitation of ferrihydrite, as well as contributing to the formation of Fe(III) silicate complexes [34]. After introducing of Ca solution into the suspension of ferrihydrite and Fe(III) silicate complexes, the siliceous hydrogarnet phase is once again observed to form, in accordance with the prediction by thermodynamic modelling using GEMS.

Without pre-precipitation of ferrihydrite (Fe_C1 and Fe_C2), little siliceous hydrogarnet is seen after 3 h of reaction, as seen by XRD in Figs. 6 and 7. GEMS calculates the equilibrium state, and in this case the same concentrations of reactants are present but a different initial pH. As such GEMS still predicts the formation of siliceous hydrogarnet for samples Fe_C1 and Fe_C2, which XRD indicates is only a minor constituent at best. This suggests that without the pre-precipitation of ferrihydrite the reaction of C-S-H with Fe^{3+} is faster than hydrogarnet formation. Similarly, for Portland cement [6,10,35], a two-stage reaction is known, with a prior precipitation of ferrihydrite and its subsequent transformation of ferrihydrite to hydrogarnet. This process is evident in our simpler C-S-H systems; with the pre-precipitation of ferrihydrite, 3 h is sufficient for the hydrogarnet formation.

The synthetic C-S-H with and without Fe^{3+} were characterized by XRD, TGA, TEM and STEM-EDX. The results confirm that the precipitated synthetic C-S-H is the major phase of seven samples. From Table 2, we see that the Fe contents in samples are 0.010–0.014 mmol/g (0.06–0.08%) of low Fe^{3+} concentration and 0.039–0.048 mmol/g (0.22–0.27%) of high Fe^{3+} concentration. Assuming an average sample density of 2.0 g/mL, this corresponds to an average concentration between 20 mM and 28 mM for the low Fe^{3+} concentrations and between 78 mM and 96 mM for the high Fe^{3+} concentrations. This represents the iron not only in C-S-H but also in secondary phases such as the Fe-containing siliceous hydrogarnet. However, the Ca/Si ratios of precipitated synthetic C-S-H with presence of Fe^{3+} , as evidenced by ICP, are

slightly decreased when compared to the pure synthetic C-S-H. This may be by the substitution of Fe^{3+} in the C-S-H structure or interlayer or the iron could be adsorbing onto the C-S-H surface. From XRD and TGA, Fe^{3+} does not show a great effect on nucleation and growth of synthetic C-S-H (interlayer or structure), although ionic radius of Fe^{3+} (0.645 Å) is smaller than Ca^{2+} (0.99 Å) and could thus possibly substitute in the Ca sites either in the main layer structure or the newly identified bridging sites in the interlayer [15]. We can corroborate the trends observed in ICP with Ca:Si ratios analyzed from the high-resolution ^{29}Si NMR spectra shown in Fig. 12. Using the C-S-H sample synthesized in the absence of added Fe^{3+} with a Ca/Si ratio of 2 as a reference, the specification of silicates in the C-S-H phases of Fe_C1 features a lower $Q^{(1)}/Q^{(2)}$ ratio than in the reference, whereas this ratio is higher for Fe_B2. More chain-terminating $Q^{(1)}$ species indicates a greater number of defects, shorter chain segments, and consequently additional calcium and a greater Ca/Si ratio. We find that the ICP and NMR results for Fe_C1 are consistent. For Fe_B2, we find the results are in opposition: NMR indicates the C-S-H Ca/Si ratio is greater than 2, whereas the ICP analysis indicates this ratio is merely 1.2. In order to reconcile these observations, we note that the Ca/Si ratio determined by ICP includes secondary phases as well, whereas the NMR result is selective for the C-S-H phase. Given the large quantity of iron-containing siliceous hydrogarnet in the sample (which is invisible to NMR by its very high iron concentration, as suggested by its assignment to the broad rolling line shape in EPR – see below), it may be that the Ca:Si ratio of this hydrogarnet phase is low.

To analyze the incorporation of iron into the C-S-H structure itself, EPR and ^{29}Si NMR relaxation data have been used. The EPR indicates two primary iron environments: magnetically isolated, paramagnetic Fe^{3+} ions and clustered iron moieties where Fe^{3+} centers are of sufficient density to allow for spin-spin coupling of the iron centers. The isolated Fe^{3+} environments dominate the EPR spectrum of Fe_C1, whereas for Fe_B2, the clustered moieties dominate. Based on STEM-EDX and XRD, the clustered iron signal corresponds to the nanoparticles of siliceous hydrogarnet, which are probably superparamagnetic [44–46].

We find by NMR that the concentration of isolated Fe^{3+} ions in the C-S-H phase of Fe_C1 is about three times that of sample Fe_B2, despite an initially lower concentration of iron during synthesis. This is qualitatively consistent with the intensity of the feature assigned to isolated Fe^{3+} in the EPR spectra shown in Fig. 12. Since the EPR method is not selective for the C-S-H phase, this agreement would indicate that most of the isolated Fe^{3+} is contained within the C-S-H. The agreement also suggests that the iron-rich nanoparticles observed in Fe_C1 by STEM-EDX do not contribute to the ^{29}Si PRE in the C-S-H phase, despite the high interfacial volume expected on account of their small size and dispersal throughout the majority of the C-S-H foil volume. To explain this, note that magnetically dilute Fe^{3+} ions are efficient nuclear relaxation agents in high-field NMR experiments due to their relatively long electron correlation times τ_e on the order of ns [47]. Because of anti-ferromagnetic spin exchange between Fe^{3+} -O- Fe^{3+} linkages [45], however, oligomeric and polymeric iron clusters in iron-rich oxides are expected to have much shorter τ_e than magnetically isolated Fe^{3+} ions, reducing their efficacy as nuclear relaxation agents [47–49]. We are thus confident that our method determines accurately the concentration of isolated, magnetically dilute Fe^{3+} ions in the C-S-H phase.

For Fe_C1, the ^{29}Si relaxation data shows a complete loss of NMR signal as τ_z approaches 1000 s, suggesting that Fe^{3+} ions are uniformly distributed throughout the C-S-H foils, in line with the prediction of our model of PRE by Fe^{3+} . For Fe_B2, the decay predicted by our model of PRE in Fe^{3+} is too rapid at long τ_z . This may indicate a nonuniform or heterogeneous distribution of Fe^{3+} ions in the C-S-H phase, featuring relatively iron-poor regions where PRE by Fe^{3+} becomes an ineffective relaxation mechanism. Such heterogeneity may be a consequence of the pre-precipitation reaction, which forces the nucleating C-S-H to scavenge Fe^{3+} , favoring foils in proximity to iron-rich ferric precipitates. This interpretation is supported by the observation that the average iron concentration determined by ICP is three times higher for sample Fe_B2

than it is for Fe_C1. In other words, while the concentration of Fe^{3+} in the C-S-H phase of sample Fe_C1 (7.5 mM) is only a factor of three lower than the overall iron concentration (22 mM) of the sample, the concentration of Fe^{3+} in the C-S-H phase of sample Fe_B2 (2.4 mM), is over a factor of thirty times lower than its overall iron concentration (78 mM). This supports our inference from the NMR data that most of the iron in Fe_B2 is locked up in the iron-rich precipitates (siliceous hydrogarnet) seen in STEM-EDX, limiting the amount of Fe^{3+} available during C-S-H formation. The excess iron in sample Fe_C1 may be accounted for by the nascent iron-rich nanoparticles, which is likely the iron-containing siliceous hydrogarnet predicted to be stable by GEMS, and which EPR shows to be present at a low concentration (Fig. 12). Since the NMR results show that Fe^{3+} in Fe_C1 is uniformly distributed in the C-S-H phase, any iron-rich phases likely formed in such a way that iron uptake during C-S-H formation was not restricted. Indeed, it may be the other way around, with C-S-H uptake of iron limiting the formation of iron-rich nanoparticles, which would explain both the uniform distribution of C-S-H iron and the brightness nonuniformity of the STEM-EDX results on the similar sample Fe_C2, shown in Fig. 3. It may also be possible that excess iron exists as residual Fe^{3+} ions adsorbed to the surface of C-S-H foils or located in pores, but this alone does not fully explain our results.

In this study we have made a first attempt to understand the Fe^{3+} interaction with a C-S-H of a single Ca/Si ratio near 2. Recent work by Mancini et al. [50] shows similar uptake values: Fe/Si atomic ratios around 0.001 for nominal Ca/Si ratios of 1.2 and 1.5. Investigating the Fe^{3+} incorporation of precipitated C-S-H with lower Ca/Si ratios, similar to those looked at by Mancini et al., would provide further insight into the effect of Ca/Si ratio on Fe^{3+} uptake. It is also worth investigating Fe^{3+} uptake or incorporation into C-S-H in the presence of aluminium, as Al^{3+} may compete with Fe^{3+} for sites in the C-S-H structure. Recent work using the precipitation method to produce C-A-S-H samples has shown promise [51] and will be a fruitful avenue for future research.

5. Conclusions

The precipitation of synthetic C-S-H was performed via dropwise method in the presence of Fe^{3+} . The addition of Fe^{3+} to the system results in precipitation of C-S-H and sometimes iron-containing siliceous hydrogarnet, $\text{Ca}_3\text{Fe}(\text{SiO}_4)_{0.84}(\text{OH})_{4.32}$ depending on the concentration of Fe^{3+} and the pH. The formation of ferrihydrite as a pre-precipitation phase when the initial solutions before C-S-H precipitation was suggested by XRD and predicted by thermodynamic modelling. This was due to the adjustment of the pH with NaOH to control the stoichiometry of the C-S-H to be precipitated. By lowering the pH of the initial Fe^{3+} containing solution the precipitation of C-S-H in the presence of Fe^{3+} occurs without any pre-precipitation. In the presence of Fe^{3+} , the Ca/Si ratios of precipitated synthetic C-S-H are generally slightly decreased, an effect which may be due to Fe affecting the structure of C-S-H but also in part to the presence of secondary phases with relatively low Ca/Si ratios. The morphology of synthetic C-S-H we form always shows a nanofoil like morphology, regardless of Fe^{3+} concentration or pre-precipitation of ferrihydrite. EPR and ^{29}Si NMR relaxation data indicate that very small amounts of isolated (magnetically dilute) Fe^{3+} ions, not in excess of an Fe/Si ratio of 0.001, are incorporated into the C-S-H structure. These measurements do not indicate whether the iron is incorporated into the chains or is merely present in the interlayer.

The second phase of iron-containing siliceous hydrogarnet ($\text{Ca}_3\text{Fe}(\text{SiO}_4)_{0.84}(\text{OH})_{4.32}$) is clearly seen after precipitation at 4.0 mM when the Fe is in either the calcium nitrate or the sodium silicate solution before precipitation, i.e. with the prior formation of ferrihydrite. It is distributed as fine, roughly spherical nanoparticles, each less than 200 nm in diameter. The presence of Fe in these nanoparticles was confirmed by STEM-EDX. Quantitative analysis of Fe^{3+} concentration by NMR using measurements of the ^{29}Si PRE indicates isolated Fe^{3+} ions are present in the C-S-H phase but at concentrations not exceeding an Fe/Si ratio of 0.0003, suggesting the pre-precipitation of the secondary iron-rich

phases restricts iron incorporation into the C-S-H. When there is no pre-precipitation of ferrihydrite, no significant formation of $\text{Ca}_3\text{Fe}(\text{SiO}_4)_{0.84}(\text{OH})_{4.32}$ was observed at either concentration investigated within the 3 h of the precipitation experiment. However, very small (<30 nm) iron rich phases were observed in the STEM-EDX and confirmed by EPR, possibly ferrihydrite or siliceous hydrogarnet. Relative to the case of synthesis where pre-precipitation occurs, the quantitative NMR analysis here indicates a higher concentration of Fe^{3+} in the C-S-H phase, even when the overall iron content during synthesis is much lower. Thus, when solvated Fe^{3+} is freely available, Fe^{3+} uptake into C-S-H appears to be competitive with the formation of other iron-rich secondary phases.

Our results suggest that the formation of $\text{Ca}_3\text{Fe}(\text{SiO}_4)_{0.84}(\text{OH})_{4.32}$ passes through ferrihydrite as an intermediate phase and needs a longer time to reach the thermodynamic equilibrium when ferrihydrite is not initially present in the C-S-H precipitation experiments. The pathway is akin to that suggested for Portland cement systems illustrating the power of the synthetic C-S-H precipitation system for clarifying the effects of individual ions, which is not always easy to follow and discern in real cement mixes.

Declaration of competing interest

The authors declare that they have no known competing financial interests or personal relationships that could have appeared to influence the work reported in this paper.

Acknowledgments

The author gratefully acknowledges comments from Prof. Barbara Lothenbach, Prof. Karen Scrivener. The authors would like to express their gratitude to Dr. Abhishek Kumar and Dr. Aslam Khuni Mohamed for supporting the experiments. This project was funded by SCG, Co. Ltd., Thailand.

Author statement

Jirawan Siramanont: powder synthesis, powder characterization, writing original draft.

Brennan J. Walder: NMR and ESR data collection, presentation and interpretation, writing original draft, reviewing and editing.

Lyndon Emsley: supervision, reviewing and editing.

Paul Bowen: supervision, reviewing and editing.

References

- [1] M.C.G. Juenger, R. Siddique, Recent advances in understanding the role of supplementary cementitious materials in concrete, *Cem. Concr. Res.* 78 (Part A) (2015) 71–80, <https://doi.org/10.1016/j.cemconres.2015.03.018>.
- [2] K.L. Scrivener, A. Nonat, Hydration of cementitious materials, present and future, *Cem. Concr. Res.* 41 (2011) 651–665, <https://doi.org/10.1016/j.cemconres.2011.03.026>.
- [3] B.B. Sabir, S. Wild, J. Bai, Metakaolin and calcined clays as pozzolans for concrete: a review, *Cem. Concr. Compos.* 23 (2001) 441–454, [https://doi.org/10.1016/S0958-9465\(00\)00092-5](https://doi.org/10.1016/S0958-9465(00)00092-5).
- [4] N. Subramanian, *Design of Reinforced Concrete Structures*, Oxford University Press, Oxford, New York, 2014.
- [5] B. Lothenbach, K. Scrivener, R.D. Hooton, Supplementary cementitious materials, *Cem. Concr. Res.* 41 (2011) 1244–1256, <https://doi.org/10.1016/j.cemconres.2010.12.001>.
- [6] B.Z. Dilnesa, E. Wieland, B. Lothenbach, R. Dähn, K.L. Scrivener, Fe-containing phases in hydrated cements, *Cem. Concr. Res.* 58 (2014) 45–55, <https://doi.org/10.1016/j.cemconres.2013.12.012>.
- [7] B. Lothenbach, Thermodynamic equilibrium calculations in cementitious systems, *Mater. Struct.* 43 (2010) 1413–1433, <https://doi.org/10.1617/s11527-010-9592-x>.
- [8] B. Lothenbach, F. Winnefeld, Thermodynamic modelling of the hydration of Portland cement, *Cem. Concr. Res.* 36 (2006) 209–226, <https://doi.org/10.1016/j.cemconres.2005.03.001>.
- [9] B.Z. Dilnesa, B. Lothenbach, G. Le Saout, G. Renaudin, A. Mesbah, Y. Filinchuk, A. Wichser, E. Wieland, Iron in carbonate containing AFm phases, *Cem. Concr. Res.* 41 (2011) 311–323, <https://doi.org/10.1016/j.cemconres.2010.11.017>.

- [10] M. Vespa, E. Wieland, R. Dähn, B. Lothenbach, Identification of the thermodynamically stable Fe-containing phase in aged cement pastes, *J. Am. Ceram. Soc.* 98 (2015) 2286–2294, <https://doi.org/10.1111/jace.13542>.
- [11] F. Avet, R. Snellings, A. Alujas Diaz, M. Ben Haha, K. Scrivener, Development of a new rapid, relevant and reliable (R3) test method to evaluate the pozzolanic reactivity of calcined kaolinitic clays, *Cem. Concr. Res.* 85 (2016) 1–11, <https://doi.org/10.1016/j.cemconres.2016.02.015>.
- [12] A. Chakchouk, B. Samet, S. Bouaziz, Difference in pozzolanic behaviour of Tunisian clays with lime and cement, *Adv. Cem. Res.* 24 (2012) 11–22, <https://doi.org/10.1680/adcr.2012.24.1.11>.
- [13] T. Danner, H. Justnes, G. Norden, T. Østnor, Feasibility of Calcined Marl as an Alternative Pozzolanic Material, in: *Calcined Clays Sustain*, Concr, Springer, Dordrecht, 2015, pp. 67–73, https://doi.org/10.1007/978-94-017-9939-3_9.
- [14] H. Ghorbel, B. Samet, Effect of iron on pozzolanic activity of kaolin, *Constr. Build. Mater.* 44 (2013) 185–191, <https://doi.org/10.1016/j.conbuildmat.2013.02.068>.
- [15] A. Kumar, B.J. Walder, A. Kunhi Mohamed, A. Hofstetter, B. Srinivasan, A. J. Rossini, K. Scrivener, L. Emsley, P. Bowen, The atomic-level structure of cementitious calcium silicate hydrate, *J. Phys. Chem. C* 121 (2017) 17188–17196, <https://doi.org/10.1021/acs.jpcc.7b02439>.
- [16] S. Grangeon, F. Claret, C. Roos, T. Sato, S. Gaboreau, Y. Linard, Structure of nanocrystalline calcium silicate hydrates: insights from X-ray diffraction, synchrotron X-ray absorption and nuclear magnetic resonance, *J. Appl. Crystallogr.* 49 (2016) 771–783, <https://doi.org/10.1107/S1600576716003885>.
- [17] B. Lothenbach, A. Nonat, Calcium silicate hydrates: solid and liquid phase composition, *Cem. Concr. Res.* 78 (Part A) (2015) 57–70, <https://doi.org/10.1016/j.cemconres.2015.03.019>.
- [18] H.F.W. Taylor, *Cement Chemistry*, 2nd Edition, Thomas Telford, 1997.
- [19] I.G. Richardson, J. Skibsted, L. Black, R.J. Kirkpatrick, Characterisation of cement hydrate phases by TEM, NMR and Raman spectroscopy, *Adv. Cem. Res.* 22 (2010) 233–248, <https://doi.org/10.1680/adcr.2010.22.4.233>.
- [20] A.R. Brough, C.M. Dobson, I.G. Richardson, G.W. Groves, Application of selective ²⁹Si isotopic enrichment to studies of the structure of calcium silicate hydrate (C-S-H) gels, *J. Am. Ceram. Soc.* 77 (1994) 593–596, <https://doi.org/10.1111/j.1151-2916.1994.tb07034.x>.
- [21] E. L'Hôpital, B. Lothenbach, D.A. Kulik, K. Scrivener, Influence of calcium to silica ratio on aluminium uptake in calcium silicate hydrate, *Cem. Concr. Res.* 85 (2016) 111–121, <https://doi.org/10.1016/j.cemconres.2016.01.014>.
- [22] F. Ziegler, A.M. Scheidegger, C.A. Johnson, R. Dähn, E. Wieland, Sorption mechanisms of zinc to calcium silicate hydrate: X-ray absorption fine structure (XAFS) investigation, *Environ. Sci. Technol.* 35 (2001) 1550–1555, <https://doi.org/10.1021/es001437+>.
- [23] D.A. Kulik, Improving the structural consistency of C-S-H solid solution thermodynamic models, *Cem. Concr. Res.* 41 (2011) 477–495, <https://doi.org/10.1016/j.cemconres.2011.01.012>.
- [24] D.A. Kulik, T. Wagner, S.V. Dmytrieva, G. Kosakowski, F.F. Hingerl, K. V. Chudnenko, U.R. Berner, GEM-Selektor geochemical modeling package: revised algorithm and GEMS3K numerical kernel for coupled simulation codes, *Comput. Geosci.* 17 (2013) 1–24, <https://doi.org/10.1007/s10596-012-9310-6>.
- [25] S. Meiboom, D. Gill, Modified spin-echo method for measuring nuclear relaxation times, *Rev Sci Instrum.* 29 (1958) 688–691.
- [26] PhySy Ltd, RMN, Version 1.8, www.physyapps.com, PhySy Ltd., Grandview Heights, OH 43212, n.d.
- [27] M. Loan, O.G.M. Newman, J.B. Farrow, G.M. Parkinson, Effect of rate of crystallization on the continuous reactive crystallization of nanoscale 6-line ferrihydrite, *Cryst. Growth Des.* 8 (4) (2008) 1384–1389, <https://doi.org/10.1021/cg060620x>.
- [28] T. Nagano, Color variations associated with rapid formation of goethite from proto-ferrihydrite at pH 13 and 40 °C, *Clay Clay Miner.* 40 (1992) 600–607, <https://doi.org/10.1346/CCMN.1992.0400515>.
- [29] B.Z. Dilnesa, B. Lothenbach, G. Renaudin, A. Wichser, D. Kulik, Synthesis and characterization of hydrogarnet Ca₃(Al_xFe_{1-x})₂(SiO₄)_y(OH)₄(3-y), *Cem. Concr. Res.* 59 (2014) 96–111, <https://doi.org/10.1016/j.cemconres.2014.02.001>.
- [30] A Practical Guide to Microstructural Analysis of Cementitious Materials, CRC Press, 2017. <https://www.crcpress.com/A-Practical-Guide-to-Microstructural-Analysis-of-Cementitious-Materials/Scrivener-Snellings-Lothenbach/p/book/9781138747234>. (Accessed 18 October 2017).
- [31] G. Montes-Hernandez, P. Beck, F. Renard, E. Quirico, B. Lanson, R. Chiriac, N. Findling, Fast precipitation of acicular goethite from ferric hydroxide gel under moderate temperature (30 and 70 °C), *Cryst. Growth Des.* 11 (2011) 2264–2272, <https://doi.org/10.1021/cg1016802>.
- [32] P.C.M. Francisco, T. Sato, T. Otake, T. Kasama, Kinetics of Fe³⁺ mineral crystallization from ferrihydrite in the presence of Si at alkaline conditions and implications for nuclear waste disposal, *Am. Mineral.* 101 (2016) 2057–2069, <https://doi.org/10.2138/am-2016-5589>.
- [33] S. Das, M.J. Hendry, J. Essilfie-Dughan, Transformation of two-line ferrihydrite to goethite and hematite as a function of pH and temperature, *Environ. Sci. Technol.* 45 (2011) 268–275, <https://doi.org/10.1021/es11903y>.
- [34] G. Pokrovski, J. Schott, F. Farges, J. Hazemann, Iron (III)-silica interactions in aqueous solution: insights from X-ray absorption fine structure spectroscopy, *Geochim. Cosmochim. Acta* 67 (2003) 3559–3573, [https://doi.org/10.1016/S0016-7037\(03\)00160-1](https://doi.org/10.1016/S0016-7037(03)00160-1).
- [35] R.M. Bozorth, E.F. Tilden, A.J. Williams, Anisotropy and magnetostriction of some ferrites, *Phys. Rev.* 99 (1955) 1788–1798, <https://doi.org/10.1103/PhysRev.99.1788>.
- [36] T. Castner, G.S. Newell, W.C. Holton, C.P. Slichter, Note on the paramagnetic resonance of iron in glass, *J. Chem. Phys.* 32 (1960) 668–673, <https://doi.org/10.1063/1.1730779>.
- [37] A.F. Karimova, ESR spectra and structure of the aquo complex [Fe(H₂O)₆]³⁺ in frozen aqueous solutions of ferric nitrate, *Theor. Exp. Chem.* 17 (1981) 210–213, <https://doi.org/10.1007/BF00516954>.
- [38] I. Bertini, C. Luchinat, G. Parigi, Paramagnetic constraints: an aid for quick solution structure determination of paramagnetic metalloproteins, *Concepts Magn. Reson.* 14 (2002) 259–286.
- [39] W.E. Blumberg, Nuclear spin-lattice relaxation caused by paramagnetic impurities, *Phys. Rev.* 119 (1960) 79–84, <https://doi.org/10.1103/PhysRev.119.79>.
- [40] I. Solomon, Relaxation processes in a system of two spins, *Phys. Rev.* 99 (1955) 559–565, <https://doi.org/10.1103/PhysRev.99.559>.
- [41] N. Bloembergen, L.O. Morgan, Proton relaxation times in paramagnetic solutions. Effects of electron spin relaxation, *J. Chem. Phys.* 34 (1961) 842–850, <https://doi.org/10.1063/1.1731684>.
- [42] I.J. Lowe, D. Tse, Nuclear spin-lattice relaxation via paramagnetic centers, *Phys. Rev.* 166 (1968) 279–291.
- [43] A. Labourel, Y.-W. Kim, W.L. Earl, Nuclear-spin-lattice relaxation in natural clays via paramagnetic centers, *Phys. Rev. B* 54 (1996) 9952–9959, <https://doi.org/10.1103/PhysRevB.54.9952>.
- [44] S. Bordiga, R. Buzzoni, F. Geobaldo, C. Lamberti, E. Giamello, A. Zecchina, G. Leofanti, G. Petrini, G. Tozzola, G. Vlaic, Structure and reactivity of framework and extraframework Iron in Fe-silicalite as investigated by spectroscopic and physicochemical methods, *J. Catal.* 158 (1996) 486–501, <https://doi.org/10.1006/jcat.1996.0048>.
- [45] M.S. Kumar, M. Schwidder, W. Grünert, A. Brückner, On the nature of different iron sites and their catalytic role in Fe-ZSM-5 DeNO_x catalysts: new insights by a combined EPR and UV/VIS spectroscopic approach, *J. Catal.* 227 (2004) 384–397, <https://doi.org/10.1016/j.jcat.2004.08.003>.
- [46] P. Selvam, S.E. Dapurkar, S.K. Badamali, M. Murugan, H. Kuwano, Coexistence of paramagnetic and superparamagnetic Fe(III) in mesoporous MCM-41 silicates, *Catal. Today* 68 (2001) 69–74, [https://doi.org/10.1016/S0920-5861\(01\)00292-9](https://doi.org/10.1016/S0920-5861(01)00292-9).
- [47] Pell AJ, Pintacuda G, Grey CP. Paramagnetic NMR in solution and the solid state. *Prog. Nucl. Magn. Reson. Spectrosc.* 2019 Apr; 111:1–271. DOI: <https://doi.org/10.1016/j.pnmrs.2018.05.001>.
- [48] J.D. Roberts, D. Doddrell, Nuclear magnetic resonance spectroscopy. Use of carbon-13 isotropic shifts as a probe of mechanisms of spin transmission in metal complexes. Some pyridine-type bases and triphenylphosphine complexed to nickel (II) and cobalt(II) acetylacetonates, *J. Am. Chem. Soc.* 92 (23) (1970) 6839–6844.
- [49] D. Bencini, Gatteschi, “EPR of Exchange Coupled Systems”, Chapter5, Dover Publications, 2012 (- ISBN: 10- 0486488543).
- [50] A. Mancini, E. Wieland, G. Geng, R. Dahn, J. Skibsted, B. Wehrli, B. Lothenbach Fe (III) uptake by calcium silicate hydrates, *Appl. Geochem.* 113 (2020), 104460.
- [51] A. Kunhi Mohamed, P. Moutzouri, P. Berruyer, B.J. Walder, J. Siramanont, M. Harris, S.C. Galmarini, S.C. Parker, K.L. Scrivener, L. Emsley, P. Bowen, The Atomic-Level Structure of Cementitious Calcium Aluminate Silicate Hydrate, *JACS* 142 (2020) 11060–11071, <https://doi.org/10.1021/jacs.0c02988>.